Chen, S.A., et al., 2021, Superhydrous hematite and goethite: A potential water reservoir in the red dust of Mars?: Geology, v. 49, https://doi.org/10.1130/G48929.1

Supplementary Materials for

Superhydrous Hematite and Goethite: A Potential Water Reservoir in the Red Dust of Mars?

Si Athena Chen[1]*, Peter J. Heaney[1]*, Jeffrey E. Post[2], Timothy B. Fischer[3], Peter J. Eng[4], Joanne E. Stubbs[4]

Affiliations:

[1]Department of Geosciences, Pennsylvania State University, PA 16802, USA.

[2]Department of Mineral Sciences, Smithsonian Institution, Washington, D.C. 20560, USA.

[3]Chevron, Houston, TX 77002, USA.

[4]Center for Advanced Radiation Sources, The University of Chicago, Chicago, IL 60637, USA.

[5]James Franck Institute, The University of Chicago, Chicago, IL 60637, USA.

Correspondence to: szc81@psu.edu; pjh14@psu.edu.

This PDF file includes:

Materials and Methods
Supplementary Text
Figs. S1 to S8
Tables S1 to S3

Materials

Natural Turgite or Hydrohematite

Two turgite samples from the Smithsonian Collection were examined: Turgite (Salisbury CT, USNM 121580) and Turgite (Turginsk River, Russia, USNM R2117).

Five hydrohematite hand specimens were analyzed from the F.A. Genth Collection at Penn State University (Fig. S1): Turgite from Galdmes, Spain (#255.1); Richmond, MA, USA (# 255.2); Salisbury, CT, USA (#255.3); Spadra, AR, USA (#255.4); and Marquette, MI, USA (#255.5).

We also analyzed by synchrotron XRD the type "hydrohaematite" collected by August Breithaupt in 1843 from Siebenhitz between Hof and Hirschberg, Bavaria, Germany (No. 11019, Mineralogical Collection, TU Bergakademie, Freiberg, Germany).

Natural stoichiometric hematite

One end member hematite standard from Michigan was used for FTIR and XRD (USNM B7371).

Synthetic Hydrohematite

Fresh ferrihydrite gel was prepared at room temperature as a transformation precursor of hydrohematite. First, we dissolved 2 g of iron (III) nitrate nanohydrate ($Fe(NO_3)_3 \bullet 9H_2O$) with DI water in a 25 mL graduate cylinder, resulting in 1 M iron nitrate solution. Then, we titrated 10 mL $Fe(NO_3)_3$ solution with 5 M KOH drop by drop and adjusted the gel to a desired pH in a beaker with a constantly stirring magnetic bar. The target pH ranged from 9.00 – 13.00 with 1.00 stepwise. As soon as the pH reached equilibrium, we transferred ~0.08 mL ferrihydrite gel from the beaker to a thin-walled quartz capillary by a syringe. The thin-walled quartz capillary was approximately 1.00 mm in outer diameter and 0.01 mm wall thickness produced by Charles Supper Company. The capillary was sealed by the UV-fast-cured epoxy (OG142-87, EPO-TEK) under a full wavelength UV lamp within 10 minutes. Headspace was kept between ferrihydrite gel and epoxy. Ferrihydrite gel was covered by papers to reduce the influence of UV light. The capillary was constantly rotated to ensure the epoxy full exposed and cured under the UV light. Ferrihydrite gel volume, gel aging time, and amount of headspace were maintained as similar as possible to minimize the sample variations.

Ferrihydrite will transform to hydrohematite and hydrogoethite by heating. The Fe vacancy concentration in hydrohematite will be influenced by ferrihydrite aging time, initial pH concentration and temperature. The preparation of fresh ferrihydrite is crucial for hydrohematite formation. We noticed that the aging time of ferrihydrite will influence the final Fe occupancy. The longer ferrihydrite aged, the higher the final Fe occupancy in end products. When ferrihydrite aged for 24 hours, ferrihydrite failed to transform to hydrohematite at the same temperature for fresh ferrihydrite transformation. Maximum hydrohematite will be formed at pH 10. Maximum hydrogoethite will be formed at pH 13. Higher temperature favors hematite than hydrohematite. We suggest the heating temperature for hydrohematite and hydrogoethite formation set to be lower than 200 ^{o}C. The Fe occupancy of synthetic hydrohematite in our experiments ranged from 0.80-0.90.

Methods

Chemical formula determination by electron probe microanalysis (EPMA)

Thin sections for EPMA analysis were prepared by Texas Petrographic Service, Inc. Natural samples were embedded in epoxy and singly polished as thin sections.

EPMA was performed on a Cameca SX Five Capabilities instrument at the Materials Characterization Laboratory (MCL), Pennsylvania State University (PSU). The quantitative chemical analysis was calibrated by a natural hematite standard. Quantitative analysis was achieved using wavelength dispersive spectroscopy. Line scans in EPMA used step sizes of 10 μm.

Crystal structure analysis by synchrotron X-ray diffraction and Rietveld structure refinement

Single-shot and time-resolved synchrotron X-ray diffraction patterns were collected at the GeoSoilEnviroCARS (GSECARS) 13-BM-C beamline at the Advanced Photon Source (APS), Argonne National Laboratory (ANL). The monochromatic X-ray wavelength was ~0.82 Å and varied slightly for different data collections. We calibrated the position and tilt of the detector with a LaB_6 powder standard loaded in a 0.1 mm quartz capillary. Each pattern was collected with an exposure time of 30 seconds using either a MAR 165 CCD detector or a Dectris PILATUS 1M pixel array detector. Calibration and 2D image integration were performed using the program Dioptas (Prescher and Prakapenka 2015).

To test the thermal stability of hydrohematite, we heated natural hydrohematite with a heating rate of 13 ^{o}C/min up to 90 ^{o}C, and 2 ^{o}C/min from 90 to 1000 ^{o}C. For time-resolved X-ray diffraction experiments, we loaded the natural hydrohematite powder in a 0.7 mm thin-walled quartz capillary with one end unsealed to release water when heating. An electrically resistive forced helium heater, similar to the one described by Peterson et al. (*2015*), was employed to heat the sample. The heater was placed below the capillary with the gas flowing out of a 6 mm nozzle directed perpendicular to the capillary's long dimension and centered on the region where XRD measurements were made. Temperature was measured by placing the tip of a type-K thermocouple into the center of helium gas flow approximately 3 millimeters from the heater's exit and a few millimeters from the capillary. Temperature was calibrated using phase transitions of $RbNO_3$and the melting point of metallic silver. We estimate that the temperature measured by the thermocouple was within ±1.5 °C of the temperature inside the capillary.

Each powder pattern was refined using the General Structures Analysis System (GSAS I) program (Larson, Dreele, and Alamos 2000; Toby 2001). The starting structural parameters of $R\bar{3}c$ hematite and *Pnma* goethite came from Blake et al. (1966) and Gualtieri and Venturelli (*1999*).

Mineral morphology by scanning and transmission electron microscopy

Scanning electron microscope (SEM) images were captured with a field emission Scios 2 SEM at MCL, PSU. The acceleration voltage was 5 keV and current was 50 pA.

Focused ion beam (FIB) samples were prepared from thin sections using a Helios NanoLab 660 at MCL, PSU. The Salisbury sample was prepared by staff scientist Dr. Trevor Clark and the Arkansas sample by Dr. Haiying Wang.

Selected area electron diffraction (SAED) and high-resolution transmission electron microscope (HR-TEM) analysis were performed using a FEI Talos F200X (S)TEM at MCL, PSU. The acceleration voltage was 200 kV.

Hydroxyl determination by Spectroscopic Analysis

Fourier transform infrared spectroscopy (FTIR) was performed with a Nicolet 6700 FT-IR spectrometer in the Department of Mineral Sciences, US National Museum of Natural History, Smithsonian Institution. We prepared the pellets by mixing KBr and the powdered samples. Background measurements were collected from a pure KBr pellet prepared in the same fashion as the mixed pellets. Background was subtracted to obtain FTIR spectra of the specimens.

Thermogravimetric analysis (TGA-MS)

The dehydration behavior was investigated by measuring H_2O and O_2 loss using combined thermal-gravimetric analysis and mass spectroscopy (TGA-MS). Samples were analyzed on a TA Instruments Discovery TGA 55 connected to a mass spectrometer. Calcium oxalate monohydrate ($CaC_2O_4 \cdot H_2O$) was used as a standard for calibration of the TGA and MS. The samples were heated at a rate of 13 °C/min to 90 °C, then the heating rate was slowed to 2 °C/min for the duration of the experiments (1000 °C).

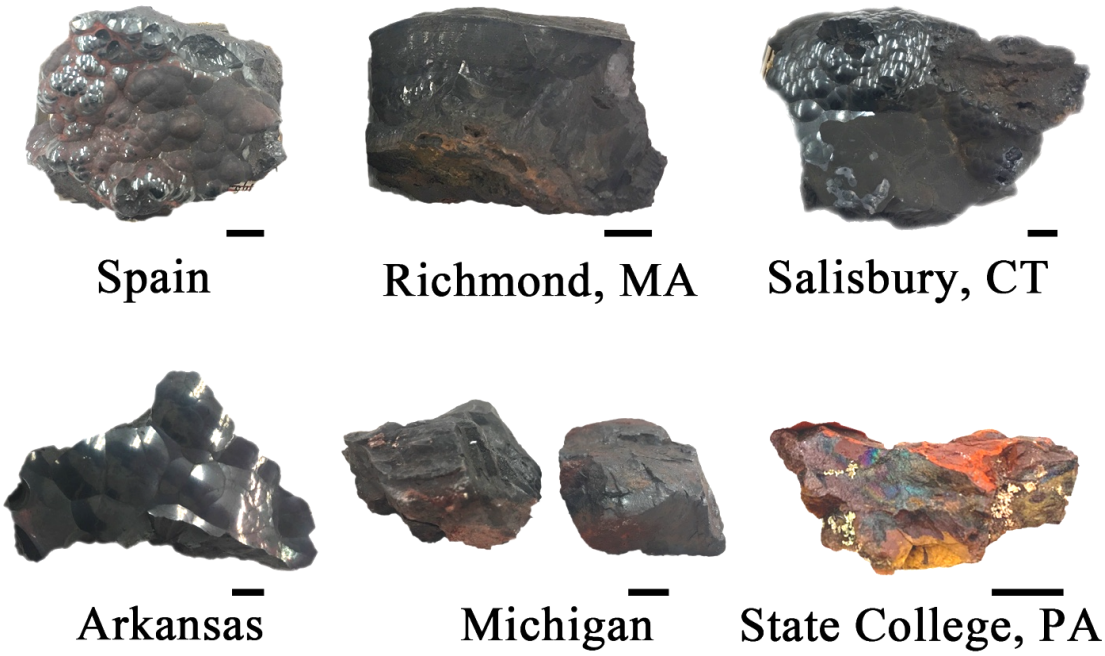

Fig. S1. Images of the "turgite" specimens from the Genth Collection at Pennsylvania State University from localities in Spain, Richmond MA, Salisbury CT, Arkansas and Michigan, and a self-collected iron ore specimen from Scotia, State College, PA. The natural hydrohematite specimens typically exhibited a botryoidal habit. Bands of hydrogoethite were intergrown with bands of hydrohematite in botryoidal specimens from Spain, Salisbury, and Arkansas. Black scale bars measure 1 cm.

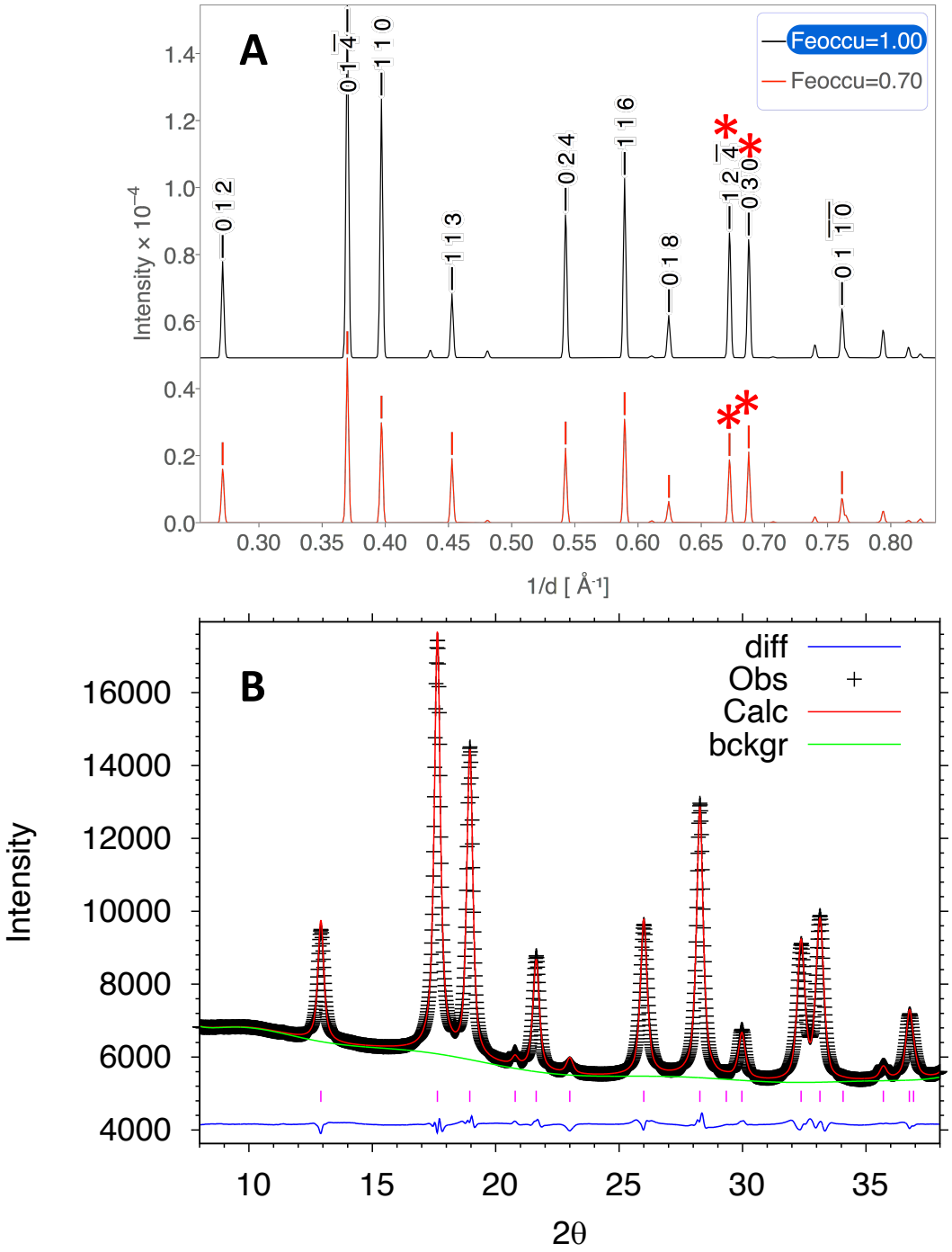

Fig. S2. (A) Simulated X-ray diffraction (XRD) patterns of stoichiometric hematite (top, black) and hydrohematite with 70% Fe occupancy (bottom, red). Variations in Fe concentration significantly influence relative peak intensities, particularly with respect to the $12\bar{4}$ and 030 peaks (starred). **(B)** Rietveld structure refinement using synchrotron powder XRD data from Salisbury hydrohematite (Genth #255.3). Fe occupancy in hematite (space group $R\bar{3}c$) was refined to be 0.825(1). Synchrotron X-ray wavelength was 0.829600 Å. Goodness of fit: χ^2= 0.3449, $R(F^2)$ = 0.0123.

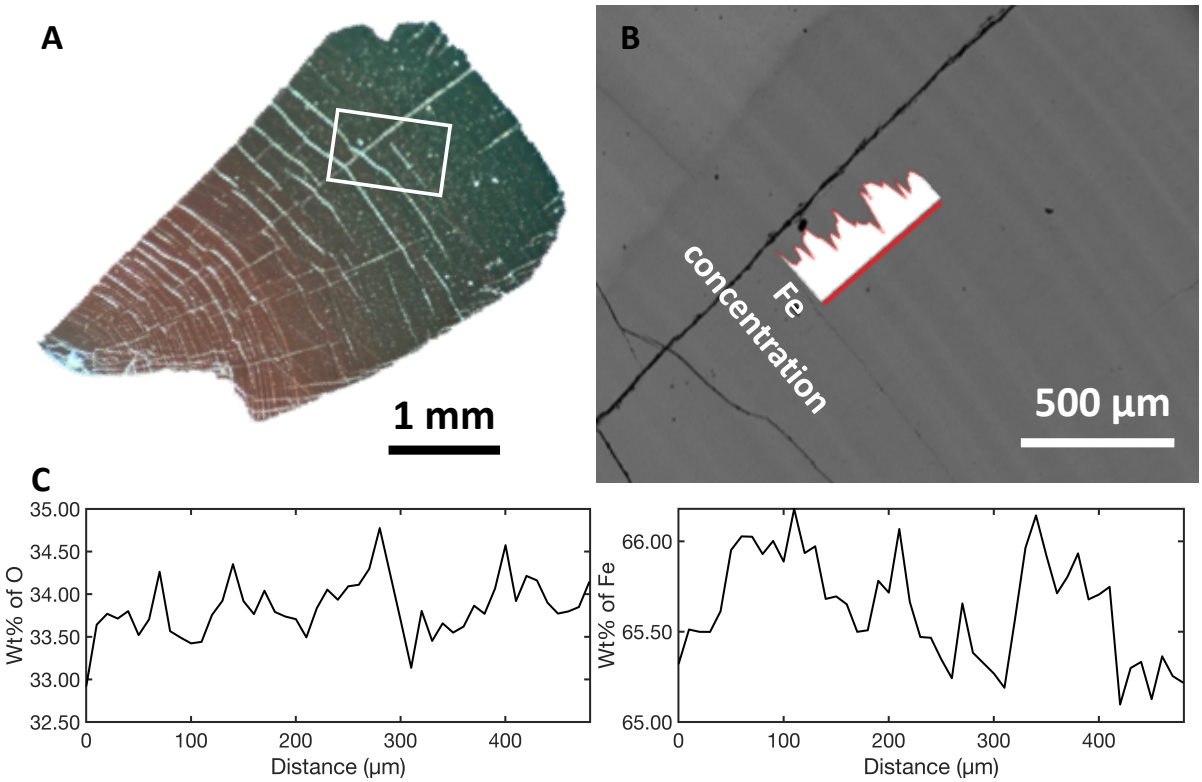

Fig. S3. EPMA quantitative analysis of natural hydrohematite from Richmond, MA, USA (Genth #255.2). (**A**) Polished thin section showing the area from which an EPMA line scan was collected. (**B**). Back-scattered electron (BSE) image showing bright and dark bands. The overlay of Fe concentration shows a strong correlation with BSE intensity. (**C**) Graphical representation of line scans across bands, revealing variations in O (left) and Fe (right) concentrations.

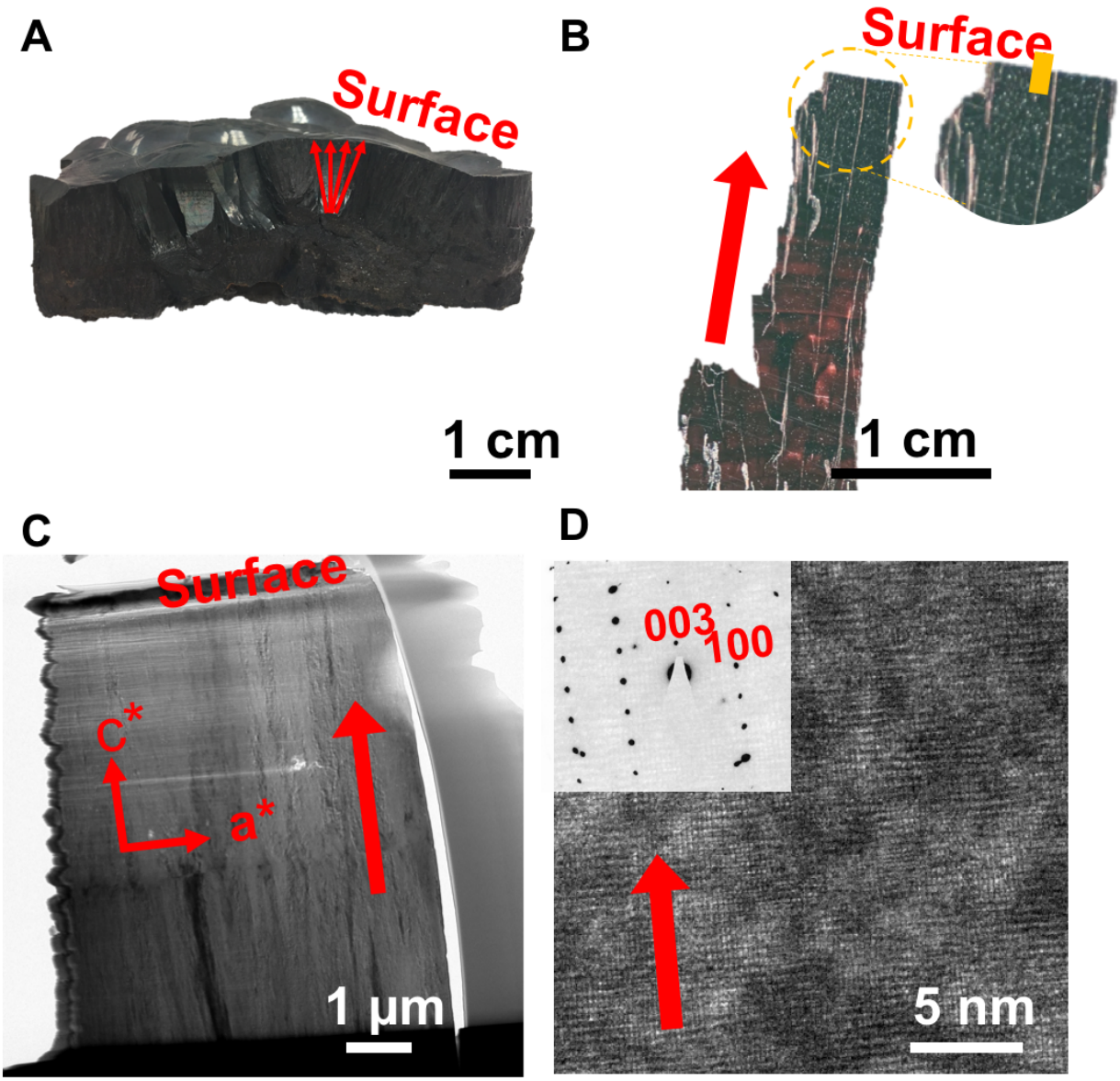

Fig. S4. Natural hydrohematite from Arkansas (Genth #255.4). Red arrows show the fiber and growth direction. (**A**) The botryoidal habit with radial fibrosity is evident in hand specimen. (**B**) A thin section was prepared along the growth direction. (**C**) A FIB-TEM sample was prepared along the growth direction and perpendicular to the surface (see the yellow rectangle in part **B**). (**D**) SAED reveals hydrohematite growth along c*. HRTEM reveals lattice continuity among nanoparticle domains.

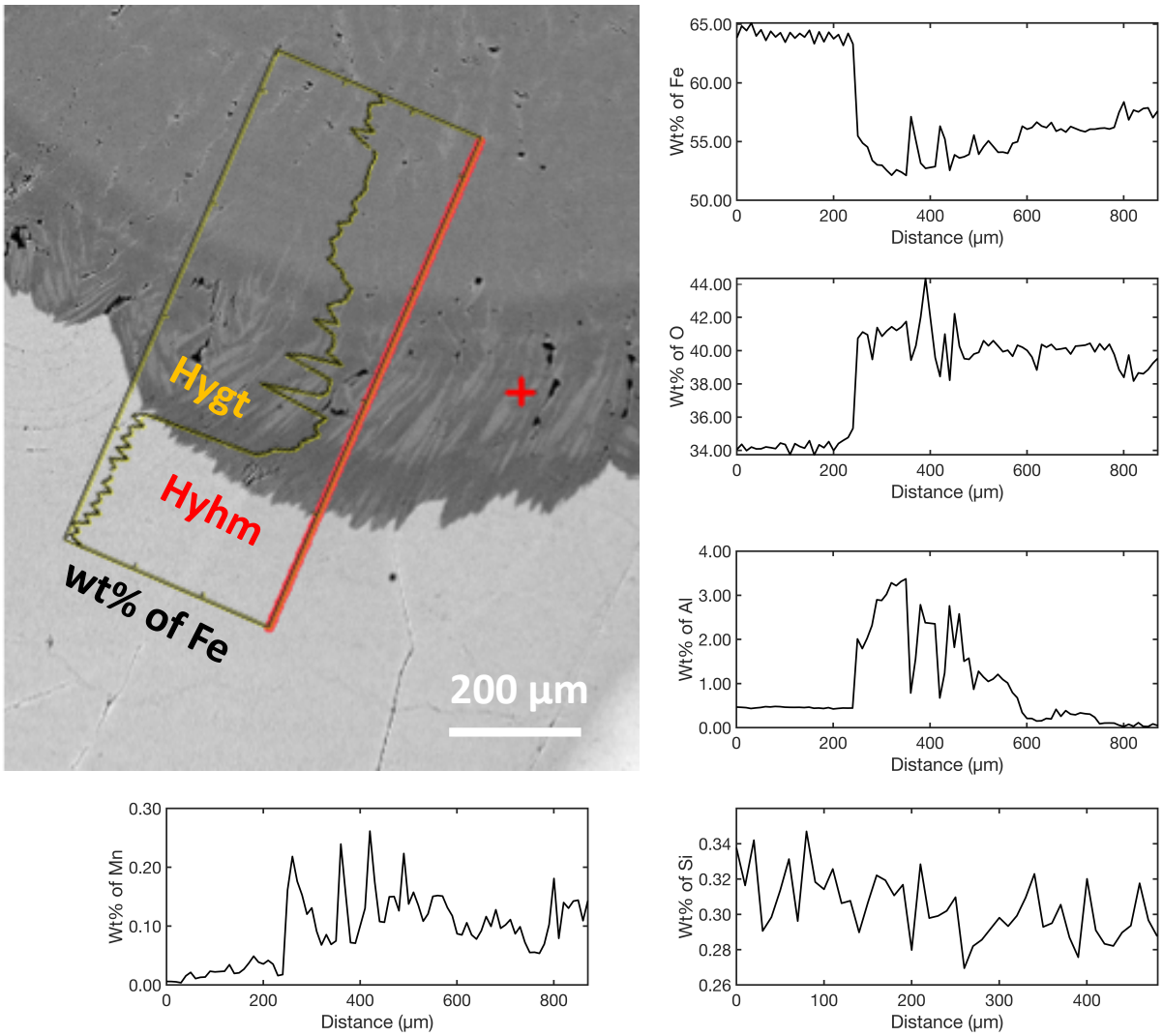

Fig. S5. EPMA line scan across the interface of hydrohematite and hydrogoethite from Salisbury, CT (Genth #255.3). Hydrohematite and hydrogoethite are intergrown as distinct bands. Very little Fe was replaced by impurity ions (e.g., Al, Si, Mg, Mn, and Cr) in hydrohematite and hydrogoethite.

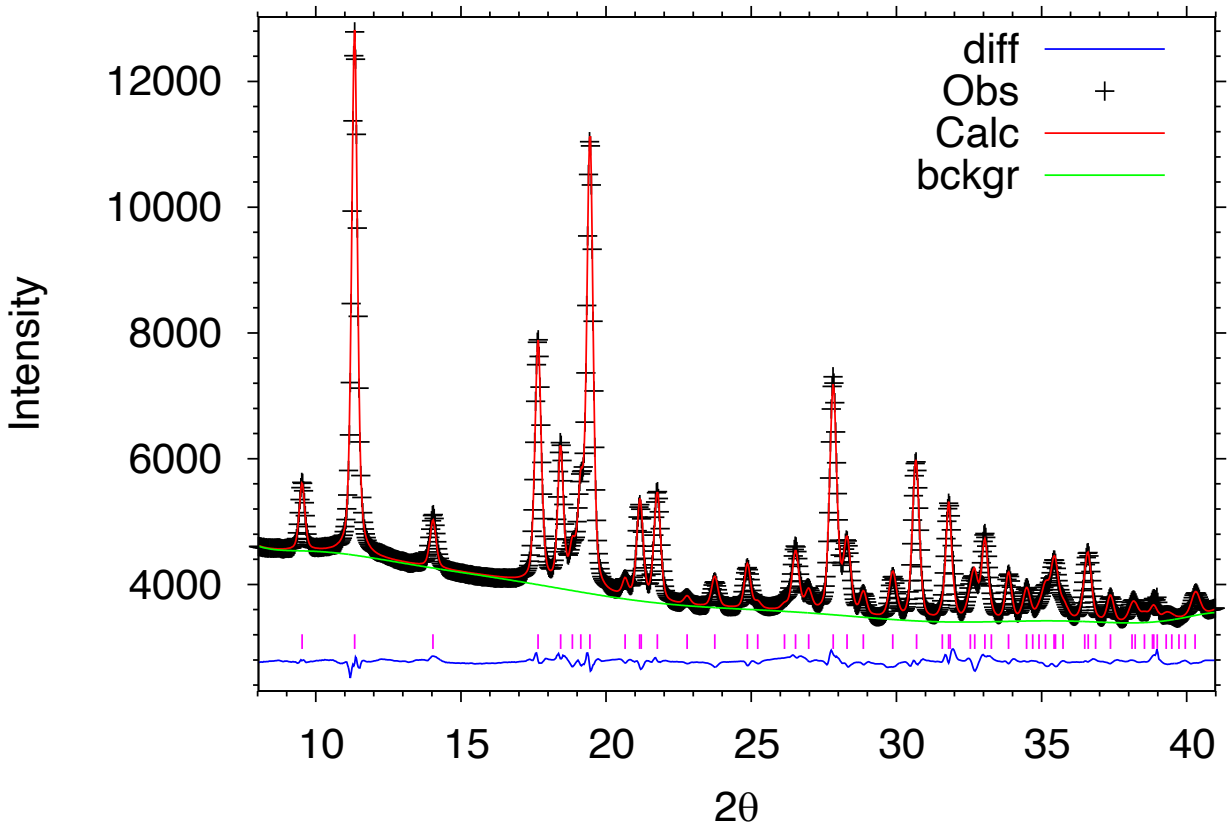

Fig. S6. Rietveld structure refinement of Salisbury hydrogoethite (Genth #255.3) using synchrotron powder XRD data. The Fe occupancy in hydrogoethite (space group *Pnma*) was refined to be 0.773(1). Synchrotron X-ray wavelength was 0.827806 Å. Goodness of fit: χ^2= 0.4149, $R(F^2)$ = 0.0449.

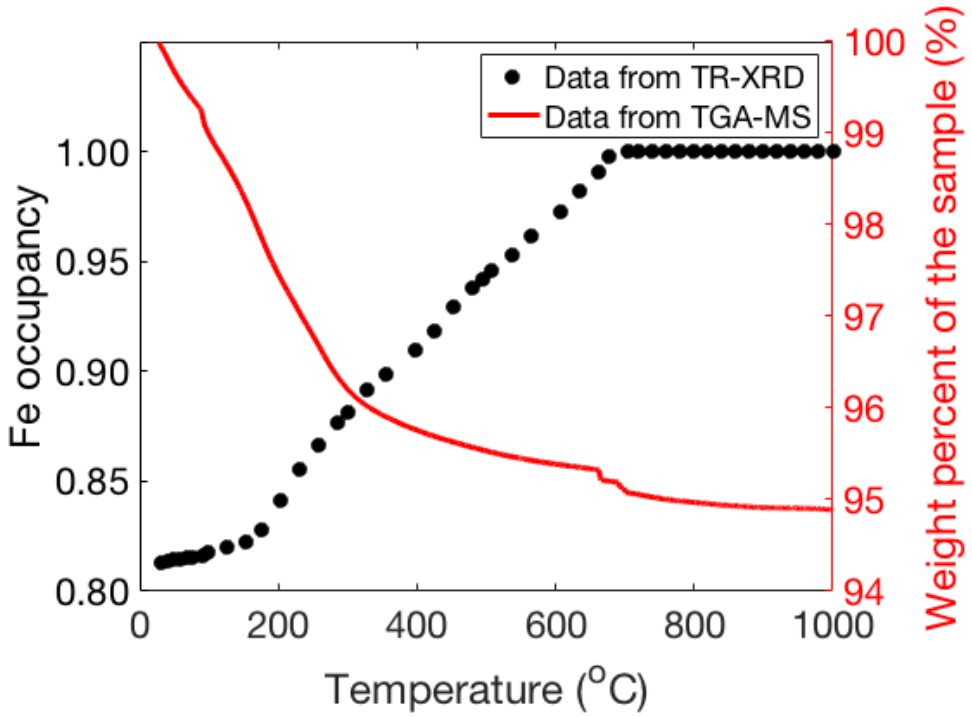

Fig. S7. Transformation of hydrohematite to stoichiometric hematite. Dry heating of Salisbury, CT hydrohematite powder (Genth #255.3) with a heating rate of 13 ºC/min up to 90 ºC and 2 ºC/min from 90 to 1000 ºC and measured by TRXRD and TGA-MS. Hydrohematite gradually transformed to hematite as indicated by an increase in Fe occupancy and evaporation of structural water. The transformation of hydrohematite to hematite was complete at ~700 ºC.

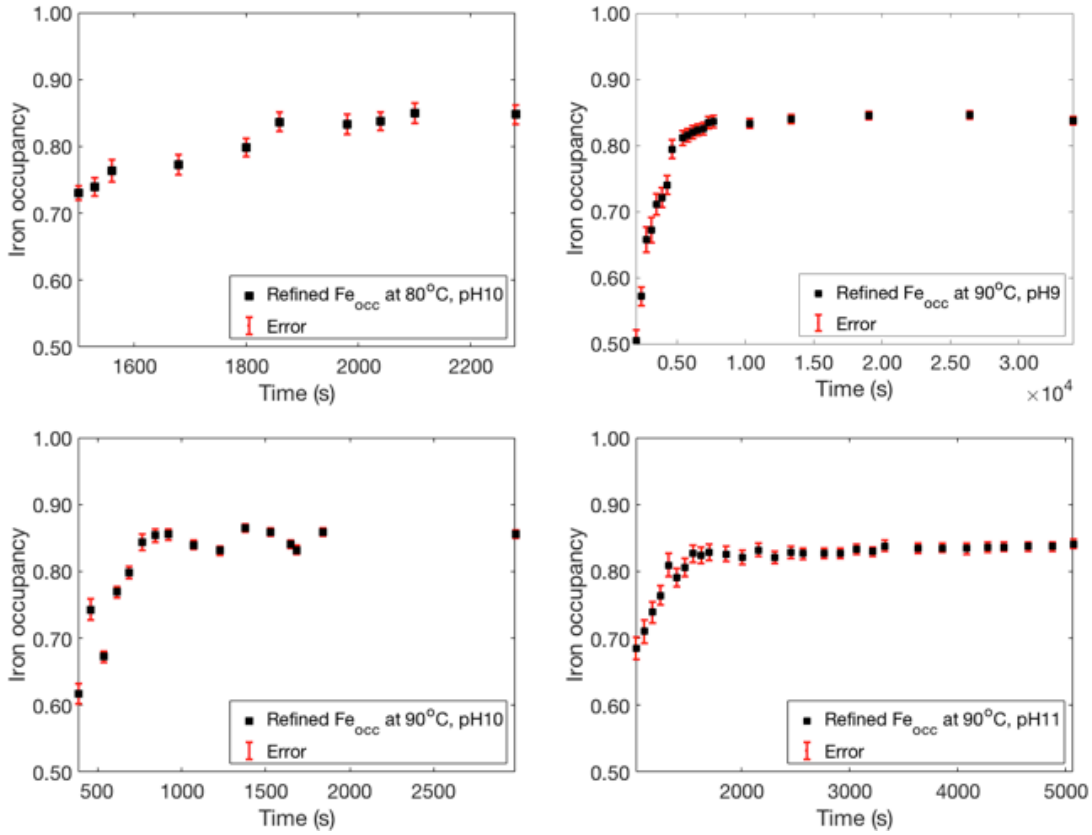

Fig. S8. Evolution of Fe occupancy in synthetic hydrohematite as a function of time at different temperatures and pH values based on Rietveld analysis of our TRXRD data. At alkaline conditions, hydrohematite evolved from a very deficient structure and stabilized with an Fe occupancy of 80-85%.

Table S1: Electron Probe Microanalysis (EPMA) of natural hydrohematite and hydrogoethite. Precision for EPMA point analysis was less than 1.0 wt%.

		Weight%											
Phase	Locality	O	Mg	Al	Si	Ca	Ti	Cr	Mn	Fe	Total	Fe occupancy	O/Fe ratio
Hematite standard	Michigan	29.85	0.00	0.01	0.03	0.04	0.05	0.06	0.08	69.93	99.82	1.00	1.49
Hydrogoethite	Spain	39.20	0.00	0.48	0.53	0.01	0.00	0.00	0.13	58.45	98.79	0.85	2.34
Hydrogoethite	Spain	40.00	0.00	0.75	0.41	0.01	0.00	0.00	0.20	58.16	99.54	0.83	2.40
Hydrohematite	Spain	34.16	-0.01	0.69	0.67	0.01	0.00	0.00	-0.01	65.10	100.61	0.82	1.83
Hydrohematite	Spain	34.33	-0.01	0.46	0.59	0.00	-0.01	0.00	0.00	65.97	101.33	0.83	1.82
Hydrohematite	Spain	34.18	0.00	0.76	0.35	0.00	0.00	0.00	0.00	64.78	100.05	0.81	1.84
Hydrogoethite	Spain	41.17	0.01	1.11	0.40	0.00	0.00	0.00	0.17	57.23	100.08	0.40	2.51
Hydrohematite	Spain	34.52	-0.01	0.77	0.43	0.01	0.00	0.01	0.01	64.59	100.33	0.80	1.87
Hydrohematite	Richmond	32.38	0.00	0.38	0.83	0.02	0.00	0.00	0.01	64.60	98.22	0.86	1.75
Hydrohematite	Richmond	33.46	0.00	0.22	0.57	0.00	0.00	0.00	0.02	65.91	100.19	0.85	1.77
Hydrohematite	Richmond	33.17	0.00	0.16	0.42	0.03	0.00	0.00	0.03	65.55	99.35	0.85	1.77
Hydrohematite	Richmond	34.37	0.01	0.07	0.28	0.00	0.00	0.00	0.03	65.05	99.80	0.81	1.84
Hydrohematite	Richmond	34.41	0.00	0.04	0.28	0.01	-0.01	0.00	0.02	65.31	100.07	0.82	1.84
Hydrohematite	Salisbury	33.07	0.00	0.47	0.98	0.02	0.00	0.00	0.00	64.46	99.01	0.84	1.79
Hydrohematite	Salisbury	35.34	0.00	0.42	1.06	0.00	0.00	0.00	0.02	63.85	100.70	0.78	1.93
Hydrogoethite	Salisbury	40.42	0.00	0.81	1.20	0.00	0.00	0.00	0.22	56.36	99.00	0.80	2.50
Hydrogoethite	Salisbury	39.77	0.00	0.11	1.55	0.00	0.00	0.00	0.08	57.05	98.55	0.82	2.43
Hydrogoethite	Salisbury	39.57	0.01	0.05	1.46	0.00	0.00	0.00	0.05	57.70	98.83	0.84	2.39
Hydrogoethite	Salisbury	39.59	0.01	0.03	1.55	0.01	-0.01	0.00	0.08	57.50	98.77	0.83	2.40
Hydrogoethite	Salisbury	40.74	0.00	0.03	1.61	0.01	0.00	0.00	0.09	57.78	100.24	0.81	2.46
Hydrohematite	Arkansas	34.25	0.00	0.41	0.94	0.01	0.00	0.00	0.00	64.19	99.79	0.81	1.86
Hydrohematite	Arkansas	34.61	-0.02	0.42	0.95	0.00	0.00	0.00	-0.01	65.39	101.34	0.81	1.85
Hydrohematite	Arkansas	34.38	0.00	0.42	0.89	0.00	0.00	0.01	-0.01	64.83	100.53	0.81	1.85
Hydrohematite	Arkansas	34.04	0.00	0.42	0.84	-0.01	-0.01	0.00	0.00	65.60	100.87	0.83	1.81
Hydrohematite	Arkansas	34.79	0.01	0.47	0.89	0.00	0.00	0.00	-0.01	64.93	101.08	0.80	1.87

Hydrohematite	Arkansas	34.44	0.00	0.63	1.03	0.00	0.00	0.01	0.00	65.30	101.40	0.81	1.84
Hydrohematite	Michigan	32.63	0.01	0.79	1.17	0.09	0.00	0.01	0.69	64.57	99.96	0.85	1.76
Hydrohematite	Michigan	32.54	0.00	0.79	1.24	0.09	0.00	0.00	0.58	65.27	100.51	0.86	1.74
Hydrohematite	Michigan	32.97	0.01	0.82	1.27	0.10	0.00	0.00	0.65	65.35	101.18	0.85	1.76
Hydrohematite	Michigan	33.21	0.01	0.58	1.03	0.06	0.00	0.00	0.50	66.31	101.71	0.86	1.75
Hydrohematite	Michigan	32.91	0.01	0.77	1.25	0.08	0.00	0.00	0.57	65.48	101.08	0.85	1.75

Table S2: Rietveld structural refinement of natural and synthetic hydrohematite.

Sample	Fe_{occ}	a=b (Å)	c (Å)	Volume ($Å^3$)	Fe-Fe (Å)	Fe-O1* (Å)	Fe-O2* (Å)	Octahedral Tilting Distortion Δ (%)†
Galdames,Spain; Hyhm	0.82(2)	5.029(1)	13.761(1)	301.42(2)	2.831(1)	2.147(1)	1.921(1)	0.0271
Richmond, MA; Hyhm	0.82(2)	5.028(1)	13.763(1)	301.38(2)	2.844(1)	2.145(1)	1.922(1)	0.0271
Salisbury, CT; Hyhm	0.83(2)	5.040(1)	13.797(1)	303.48(2)	2.847(1)	2.154(1)	1.923(1)	0.0270
Arkansas; Hyhm	0.80(2)	5.028(1)	13.765(1)	301.40(2)	2.819(1)	2.143(1)	1.923(1)	0.0270
Syn hyhm‡	0.83(2)	5.041(1)	13.778(1)	303.21(2)	2.872(1)	2.167(1)	1.914(1)	0.0270
Hematite§	1.00	5.038(2)	13.772(12)	302.72(30)	2.971(1)	2.116(2)	1.946(2)	0.0291

*Within the FeO_6 octahedra, longer Fe-O bond labeled as Fe-O1 in this paper and shorter labeled as Fe-O2. † Octahedral tilting distortion (Δ) is calculated by OctaDist program, where $\Delta = \frac{1}{6}\Sigma(\frac{di-dmean}{dmean})^2$ where d_i is the individual bond length and d_{mean} is the average bond length (Lufaso and Woodward 2004; Ketkaew et al. 2020). ‡ Synthetic hydrohematite (Syn hyhm) was prepared by heating the ferrihydrite gel at pH concentration 11, constant temperature at 90 °C, and at t = 1 hr from our TRXRD experiment. §Stoichiometric natural hematite structure from (Blake et al. 1966).

Table S3: Refined crystal structure of natural hydrohematite based on synchrotron XRD.

Sample	Locality	a=b (Å)	c (Å)	Volume (Å^3)	Iron occupancy
Genth #255.1	Spain	5.029(1)	13.761(1)	301.42(2)	0.822(1)
Genth #255.2	Richmond	5.028(1)	13.763(1)	301.38(2)	0.829(1)
Genth #255.3	Salisbury	5.040(1)	13.797(1)	303.48(2)	0.825(1)
Genth #255.4	Arkansas	5.028(1)	13.765(1)	301.40(2)	0.809(1)
Genth #255.5	Michigan	5.022(1)	13.718(1)	299.65(2)	0.806(1)
Synthetic hydrohematite	Lab synthetic, 90 °C, pH11	5.041(1)	13.778(1)	303.21(2)	0.837(1)

Table S4: Refined crystal structure of natural hydrogoethite based on synchrotron XRD.

Sample	Locality	a (Å)	b (Å)	c (Å)	Volume (Å^3)	Iron occupancy
Genth #255.1	Spain	9.964(1)	3.024(1)	4.612(1)	139.01(2)	0.813(1)
Genth #255.3	Salisbury	9.963(1)	3.021(1)	4.616(1)	138.97(2)	0.773(1)
Genth #255.4	Arkansas	9.925(1)	3.012(1)	4.600(1)	137.55(2)	0.846(1)

References

Blake, R. L., R. E. HessevicK, T. Zoltai, and L. W. Finger. 1966. “Refinement of the Hematite Structure.” *American Mineralogist* 51: 123–29.

Ketkaew, Rangsiman, Yuthana Tantirungrotechai, Phimphaka Harding, Guillaume Chastanet, Philippe Guionneau, Mathieu Marchivie, and David J Harding. 2020. “OctaDist: A Tool for Calculating Distortion Parameters in Spin Crossover and Coordination Complexes.” *Dalton Transactions*.

Larson, Allen C, Robert B Von Dreele, and Los Alamos. 2000. “General Structure Analysis System.” *Structure*.

Lufaso, Michael W., and Patrick M. Woodward. 2004. “Jahn-Teller Distortions, Cation Ordering and Octahedral Tilting in Perovskites.” *Acta Crystallographica Section B: Structural Science* 60 (1): 10–20. https://doi.org/10.1107/S0108768103026661.

Prescher, Clemens, and Vitali B. Prakapenka. 2015. “DIOPTAS: A Program for Reduction of Two-Dimensional X-Ray Diffraction Data and Data Exploration.” *High Pressure Research* 35 (3): 223–30. https://doi.org/10.1080/08957959.2015.1059835.

Toby, Brian H. 2001. “General Structure Analysis System - GSAS / EXPGUI, A Graphical User Interface for GSAS.” *J. Appl. Crystallogr.* 34 (1994): 210–13. https://doi.org/10.1007/s10701-007-9105-0.